CLICdp-Note-2018-008
12 December 2018
(revised 12 April 2019)

Time and Energy Calibration of Timepix3 Assemblies with Thin Silicon Sensors

F. Pitters[*†1)2)], N. Alipour Tehrani[*], D. Dannheim[*], A. Fiergolski[*], D. Hynds[*3)], W. Klempt[*], X. Llopart[*], M. Munker[*], A. Nürnberg[*4)], S. Spannnagel[*], M. Williams[*‡]

[*] *CERN, Switzerland,* [†] *TU Wien, Austria,* [‡] *University of Glasgow, Great Britain*

Abstract

The Timepix3 ASIC is a multi-purpose readout chip for hybrid pixel detectors. It can measure time and energy simultaneously by employing time-of-arrival (ToA) and time-over-threshold (ToT) techniques. In the presented work, a time efficient method for pixel-by-pixel calibration of both ToA and ToT is investigated. Five assemblies of Timepix3 ASICs bump bonded to silicon pixel sensors of different thicknesses between 50 µm and 150 µm are calibrated with electrical test pulses, x-ray fluorescence and beams of minimum ionising particles in a reference telescope. After calibration, the energy resolution at 6.40 keV is 9.3 %. For 120 GeV/c pions, time resolutions down to 0.72 ns are achieved.

This work was carried out in the framework of the CLICdp Collaboration

[1] Corresponding author: florian.pitters@cern.ch
[2] Now at HEPHY, Austria
[3] Now at NIKHEF, The Netherlands
[4] Now at KIT, Germany

Contents

1. Introduction

Timepix3 is a multi-purpose readout ASIC [1] for hybrid pixel detectors. It can measure time and energy simultaneously by employing time-of-arrival (ToA) and time-over-threshold (ToT) techniques. The non-linear behaviour of both methods makes a pixel-by-pixel calibration with monochromatic x-ray sources time consuming and cumbersome due to the small pixel size and the many energy points required.

In the presented work, a time efficient method for pixel-by-pixel calibration of both ToT and ToA is investigated and a full calibration procedure for the Timepix3 chip is suggested. It relies on a combination of test pulse injection and source or beam measurements. Five assemblies of Timepix3 ASICs bump bonded to silicon pixel sensors of different thicknesses between 50 µm and 150 µm are calibrated and measured in particle beams.

In Sec. 2, the experimental setup of ASIC, sensor and further readout is described. Sec. 3 deals with the general characteristics of the ASIC such as noise and threshold dispersion. Sec. 4 describes the calibration procedure while Sec. 5 shows the impact of the calibration on uniformity, energy resolution and time resolution.

2. Experimental Setup

2.1. The Timepix3 ASIC

The Timepix3 ASIC consists of a 256 by 256 pixel matrix with 55 µm pixel pitch. A simplified pixel layout of the ASIC is shown in Fig. 1. Each pixel consists of a charge sensitive amplifier (CSA) with a feedback capacitor for amplification and shaping of the input signal. If there is a voltage difference between the input and output node of the CSA, the capacitor is actively discharged via a current controlled by a Krummenacher feedback network [2]. The discharge current is limited by the network, resulting in a constant discharge. The CSA output is connected to a single threshold discriminator with the possibility of a 4 bit local threshold adjustment. The global threshold is controlled by two DACs (fine and coarse) that are combined and linearised. The least significant bit (LSB) of the fine DAC corresponds to 0.5 mV. The discriminator output is then sent for digital processing.

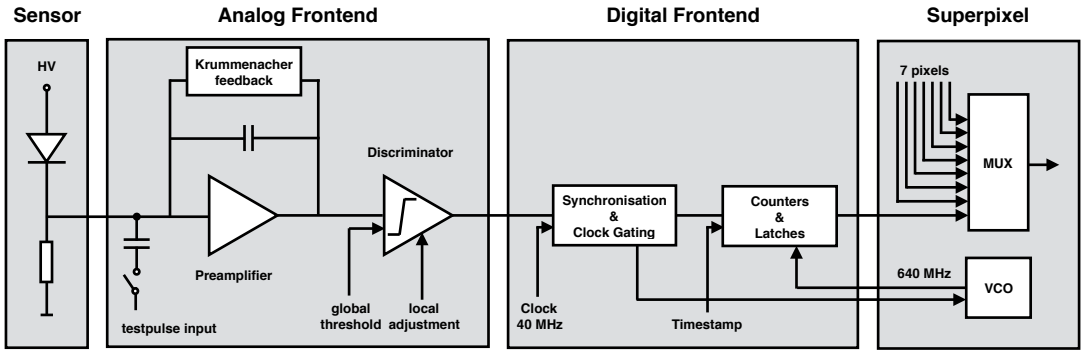

Figure 1: Schematic of the Timepix3 readout circuit. Reproduced from [1, Fig. 3] with small adaptations.

In the main operating mode used in the presented work, the ASIC employs a 10 bit time-over-threshold (ToT) and a 14 bit time-of-arrival (ToA) binary counter running at a 40 MHz clock for

simultaneous measurements of energy and time. This mode is called called ToT & ToA mode. An exemplary operating diagram is shown in Fig. 2. If the input signal rises above the constant threshold value, the discriminator starts the ToT counter which then runs until the signal falls below the threshold again. The ToA value is taken from a free-running global Gray counter. An additional 4 bit counter runs at 640 MHz, but only until the next rising edge of the 40 MHz clock. Combining the counter values for the 40 MHz global clock and 640 MHz fast clock results in a more precise time and energy measurement. A more detailed description of the ASIC can be found in [3].

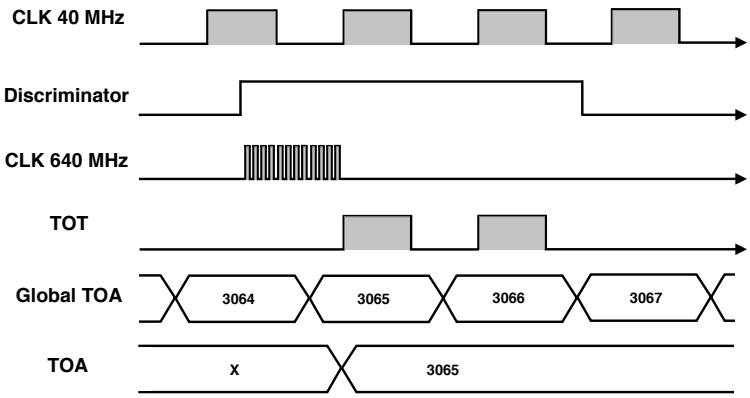

Figure 2: Operating principle of the ToT & ToA operating mode. Reproduced from [1, Fig. 4] with small adaptations.

Alternatively, the ASIC can be configured to operate in photon counting and integrated ToT (PC & iToT) mode in which the total number of hits above threshold and the integral ToT of those hits are recorded. In the presented work, this mode of operation is used for noise measurements and threshold scans.

Each block of 2x4 pixels makes up a super-pixel sharing a range of common infrastructure, most importantly the same voltage-controlled oscillator (VCO) that delivers the 640 MHz clock. Additionally, a set of 2x16 pixels share, among others, the clock buffer.

2.1.1. Time Measurement

The signal rise time is independent of the signal height. Therefore, a signal with a large amplitude crosses the constant value threshold earlier than a signal with a smaller amplitude. This phenomenon is commonly called timewalk. The shift in time $f_{\mathrm{toa}}(x)$ with amplitude x can be modelled with

$$f_{\mathrm{toa}}(x) = \frac{c_{\mathrm{toa}}}{x - t_{\mathrm{toa}}} + d_{\mathrm{toa}}. \tag{1}$$

This function is motivated by trigonometric considerations as described in App. A. The three free parameters c_{toa}, t_{toa} and d_{toa}, correspond to the curvature, the asymptote and the offset of the response function.

2.1.2. Energy Measurement

The same phenomenon that causes timewalk, also causes a non-linear behaviour of the energy response on the signal amplitude close to the threshold. With x again representing the signal

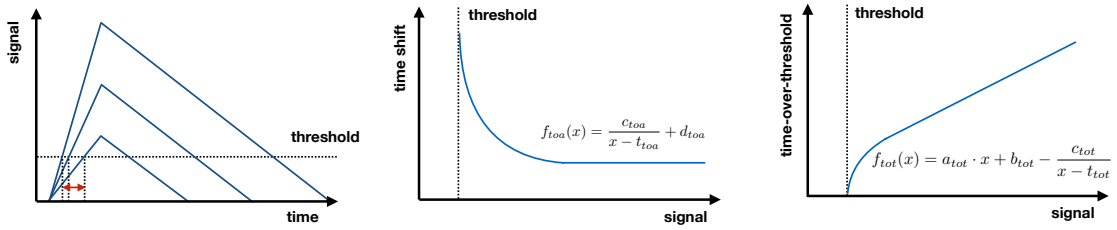

(a) (b) (c)

Figure 3: Timewalk effect (a) resulting from signals with different amplitudes but constant rise time crossing a constant threshold on the ToA (b) and ToT (c) response.

amplitude, the energy response $f_{\text{tot}}(x)$ can be modelled with

$$f_{\text{tot}}(x) = a_{\text{tot}} \cdot x + b_{\text{tot}} - \frac{c_{\text{tot}}}{x - t_{\text{tot}}}. \tag{2}$$

The free parameters a_{tot} and b_{tot} correspond to the gain and offset of the linear part while c_{tot} and t_{tot} again describe the curvature and asymptote of the non-linear part. The effect of timewalk on both ToA and ToT is sketched in Fig. 3.

The gain and dynamic range of this measurement can be controlled via the discharge current i_{krum} of the Krummenacher network. It can be controlled by a 7 bit DAC. This value is a trade-off between precision and temperature stability: A smaller discharge current can in principle increase the precision of the energy measurement but requires a more stringent temperature control. For the chosen value, a change in gain of about 3 % over 20 °C has been observed. The current also determines the dynamic range of the readout. For the presented work, this DAC value was set to 10 which corresponds to a total dynamic range of roughly 150k electrons. The temperature was controlled with a fan to about ± 1 °C. If not stated otherwise, the operating temperature was 54 °C.

2.2. The Sensor

The Timepix3 ASIC is bump-bonded to a silicon pixel sensor of the same pixel pitch as the ASIC. In the presented work, five different n-on-p sensors with active edge processing and different thicknesses are investigated. The list of assemblies is shown in Tab. 1. The naming scheme is based on the ASIC and consists of the wafer number (e.g. W19) followed by the position of the ASIC on the wafer (e.g. C7). The nominal operating voltage is set to be approximately 5 V above the depletion voltage. The nominal operating threshold was obtained from noise and baseline measurements explained in the following sections.

2.3. Test Pulse Injection Input

Each pixel of the ASIC foresees the possibility for test pulse injection. Here, a step voltage is injected via an input capacitor that is connected in parallel to the sensor input. The design value of this capacitor is 3 fF. The injection input can be activated and deactivated separately for each pixel. An ADC allows to measure the applied voltage. The pulse generator as well as the ADC are global to the ASIC and located at the periphery. Therefore, the voltage that is actually applied to the input capacitor at each pixel is not a priori known. There is also the option to inject the test pulse directly into the digital frontend, bypassing the preamplifier and discriminator (digital test pulse).

Table 1: List of assemblies and their nominal operating conditions used in the presented work.

Chip ID [-]	Sensor Thickness [um]	Type [-]	Nom. Op. Voltage [V]	Nom. Threshold [LSB]
W19_C7	50	n-on-p	-15	1190
W19_F7	50	n-on-p	-15	1187
W19_G7	50	n-on-p	-15	1148
W5_E2	100	n-on-p	-20	1160
W5_F1	150	n-on-p	-30	1153

2.4. Other Elements of the Readout Chain

The assembly is wire-bonded to a readout PCB, the chip board, that handles mainly the power distribution for the ASIC and the bias voltage supply for the sensor. The chip board is then connected via an FMC connector to the SPIDR readout board [4]. There, an FPGA handles data acquisition and slow control. A TDC channel with a precision of about 250 ps [4] is available for an external trigger input. The data is then transmitted via a 10 Gbit Ethernet connection to a PC.

2.5. Xray Tube Setup

For the energy calibration, measurements in an x-ray tube have been conducted. Here, electrons from a thin filament are accelerated to 40 keV by an electrostatic field, focused and sent onto an external target material. The resulting fluorescent x-rays are measured with a Timepix3 assembly. The setup is shown in Fig. 4.

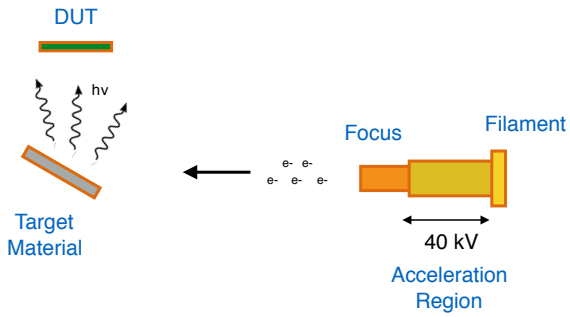

Figure 4: Schematic of the setup used for x-ray tube measurements.

2.6. Testbeam Setup

Beam tests have been conducted in the SPS H6 beamline with 120 GeV incident pions. In October 2015, assemblies have been measured in the CLICdp Timepix3 telescope shown in Fig. 5. The telescope employs 6 tracking planes, 3 upstream and 3 downstream of the DUT. It delivers a pointing resolution at the DUT position of about 1.8 µm and a track time resolution of about 1 ns [5]. Two organic scintillators with PMT readout in front and in the rear, can be

used to obtain a more precise reference timestamp. The telescope itself is not triggered but rather all recorded hits are read out and matched offline. Hits on the scintillators are only read out if they are recorded in coincidence. They are then sampled by the trigger input of the first SPIDR board.

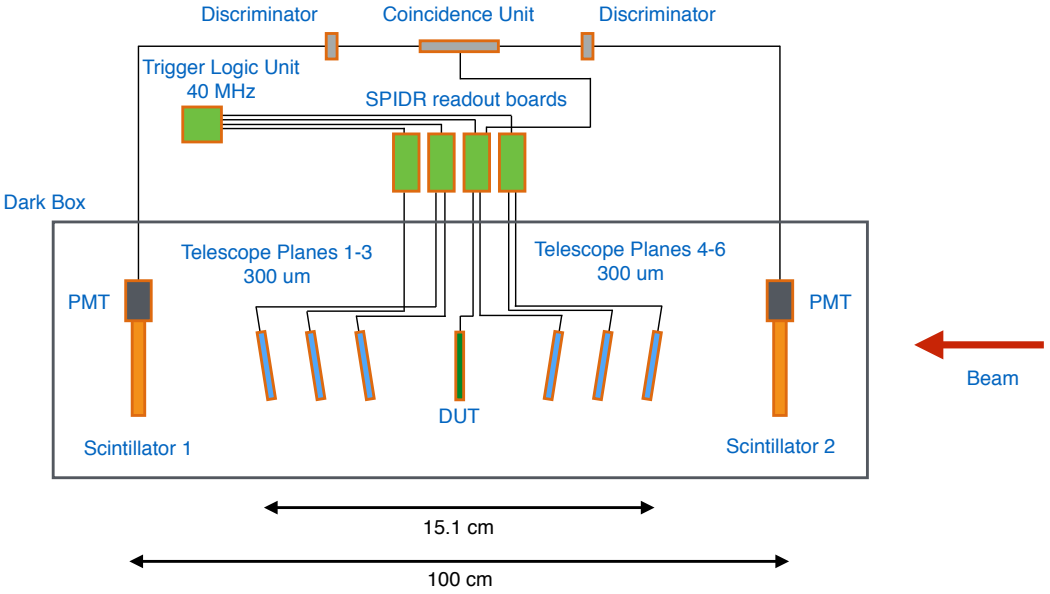

Figure 5: Schematic of the telescope setup and readout used for beam tests.

Tracking and reconstruction is done within the Corryvreckan framework [6]. The event stream is divided into slices of 25 µs. Clusters on the 6 planes that pass a timing cut of 200 ns and a spatial cut of 200 µm are associated with a track candidate and reconstructed with a straight line fit. If the fit passes a χ^2/ndof cut of 3 it is considered a track. Within the 25 µs, on average 8 tracks are found. Three timestamps can then be extracted from track, scintillators and DUT. The track timestamp is taken as the average of the 6 associated clusters on the 6 telescope planes, corrected for average time-of-flight and latencies. Per cluster, the timestamp of the most energetic pixel is used as cluster timestamp to minimise the influence of diffusion. The DUT timestamp is obtained in the same way. Lastly, a coincidence scintillator timestamp is associated with a track if one can be found within a window of ±7 ns around the track timestamp.

The scintillator has a better time resolution than the telescope tracks and is therefore the preferred time reference. However, due to the low efficiency of the scintillators (about 75% per layer according to lab measurements with cosmics) and the untriggered data stream, the finite window length is necessary to avoid association with a wrong track. The value of 7 ns is motivated by Fig. 6 which shows the RMS of the time difference between track and DUT for different window lengths as well as the probability of finding a coincident scintillator hit within that window. Since the 3 timestamps are all independent, the window length used to search for a scintillator timestamp can not bias the measured RMS between track and DUT timestamps. 7 ns is the smallest value that fulfils this criterion. The probability of finding a coincident scintillator hit within this window is 61%, slightly better than what is expected from lab measurements. At smaller windows, the probability and RMS of the residual distribution starts to drop and at windows larger than 50 ns the probability rises due to mis-association.

The scintillator timestamp is then used as a time reference and tracks are used only as position reference. Tracks without associated scintillator hits are discarded from the analysis.

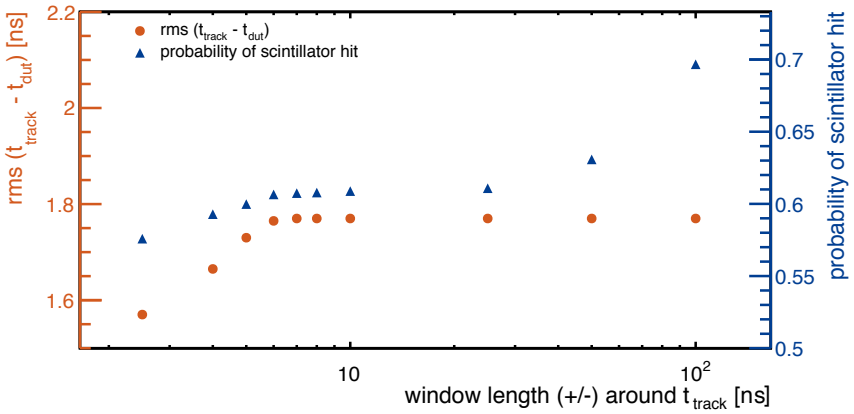

Figure 6: Influence of the search window used to search for a scintillator timestamp on the measured RMS between track and DUT timestamps.

2.7. Box Plot Conventions Used for this Work

Many results in the presented work are shown as box plots. For these plots, the median of the distribution is represented by a solid line, the mean by a dashed line. The box boundary represents the inter-quartile range, i.e. the middle 50% of the distribution (which corresponds to 1.349 σ). The whiskers are at 2.5 times the inter-quartile range and contain 5.396 σ or 98.95% of all data points. For more details on this form of representation the reader is referred to [7].

3. General Characteristics of the ASIC

3.1. Threshold Variations and Equalisation

During the wafer production, process variations can lead to differences in behaviour across the ASIC. For an energy measurement based on time-over-threshold, pixel-to-pixel variations of the threshold are particularly relevant because they result in different turn-on points. Similarly, a time measurement based on time-of-arrival will suffer from an additional delay that varies from pixel to pixel and, if not corrected for, will result in an additional source of uncertainty on the time resolution. To counteract pixel-to-pixel variations in the effective threshold, the Timepix3 ASIC employs a local voltage correction to the global threshold. This 4 bit adjustment setting is called *trim DAC*. The goal of the threshold equalisation is to find the set of trim DACs that minimises the dispersion of the effective threshold across the pixel matrix.

Due to gain dispersion, the equalisation should be done ideally at the operating threshold of the assembly. However, for practical reasons this is often not possible.[5] In the presented work, the ASIC is equalised at the edge of the noise floor defined as the first threshold setting that records more than 10 noise hits in a time of 1 ms. The equalisation is then achieved by the following procedure.

[5] It can be done e.g. via test pulse injection. However, the authors found that it does not yield superior results while increasing the equalisation time by roughly two orders of magnitude.

1. Set the trim DAC setting for all pixels to the minimum value (0x0) and do a threshold scan for the noise edge. Repeat the procedure with the maximum trim DAC value (0xF). The result are two broad distributions representing the noise edge position in units of the global threshold DAC for all pixels in the matrix.

2. Extract the global average threshold at trim DAC 0x0 and 0xF as the means of the two distributions. Set a first equalisation target as midpoint between the two global threshold values. For each pixel, interpolate to find the trim DAC setting closest to that target.

3. Scan again for the noise edge and set the refined equalisation target as the mean of the new distribution. For each pixel, see if a better trim DAC setting can be found and scan again for the noise edge.

4. Iterate the last point until no change is observed anymore. Typically, one iteration is enough.

The measured noise edge dispersion before and after the equalisation is shown in Fig. 7. It is notable that the distribution becomes box-like after the equalisation, indicating that the precision of the process is limited by the binning of the trim DACs (4 bit). The RMS is typically reduced by a factor 6 to 7 to about 3 LSB.

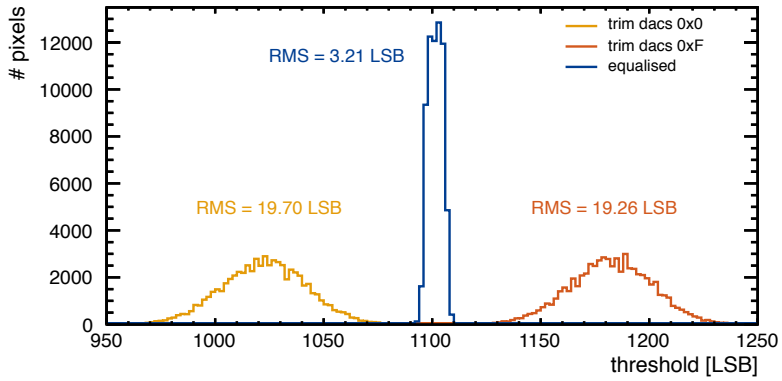

Figure 7: Illustration of the threshold equalisation. The distributions of the noise edge (see text) for trim DAC 0, trim DAC F and equalised trim DACs are shown. After equalisation, the RMS of the distribution is typically reduced by a factor 6 to 7. Assembly shown is W5_E2.

During steps 2, 3 and 4, if no trim DAC setting can be found that brings the pixel within the range of one trim DAC step to the equalisation target, the pixel is identified as noisy and masked. Additional pixels might be masked manually at later stages. In total, between 33 and 46 pixels have been masked per assembly.

3.2. Threshold Gain Measurement

To establish the gain per threshold LSB, a test pulse with a fixed amplitude is injected into one pixel frontend N times. Then a threshold scan around the expected amplitude range is performed and the number of signals seen by the frontend are counted at each threshold. The result is the cumulative distribution function (CDF) of the normal distribution. This function,

a modified error function, is given in Eq. 3 and is often called s-curve.

$$f_{\mathrm{cdf}}(x) = \frac{N}{2}\left[1 - \mathrm{erf}\left(\frac{x-\mu}{\sigma\sqrt{2}}\right)\right]. \tag{3}$$

The mean μ of this function corresponds to the test pulse signal and σ to the noise. This is repeated for three test pulse amplitudes. A linear fit is performed and the gain can be extracted. A noise scan determining the baseline is also performed but not included in the fit. The procedure is quite lengthy as only a subset of pixels can be injected at the same time to avoid crosstalk. Therefore, the gain calibration is only done for one diagonal of 256 pixels per chip.

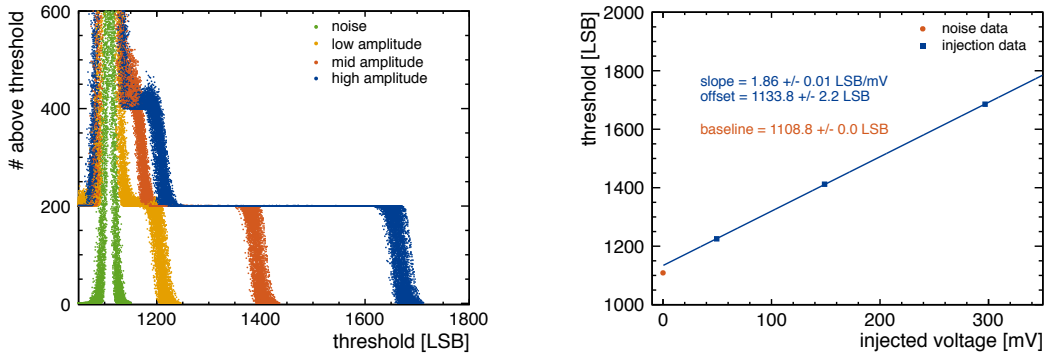

(a) (b)

Figure 8: Illustration of the threshold gain measurement. 200 test pulses are injected into 256 pixels at 3 different test pulse amplitudes (a). The colours correspond to the different amplitudes. A noise scan of the baseline is also shown. For each pixel, the s-curves are fitted with a CDF function and a linear fit is performed to extract the gain per threshold step (b). Assembly shown is W5_E2.

Fig. 8(a) shows the resulting s-curves of 200 pulses injected in each of the 256 diagonal pixels for a n-on-p sensor. The polarity of the threshold DAC is such that higher DAC value equals a higher threshold for negative input signals. Therefore, at large threshold values no pulses are seen at the input as they are all below threshold. Lowering the threshold, more and more pulses are seen until all 200 injected pulses are seen at the input.[6] Per pixel, each transition region is fitted with a CDF and the means of the curves are fitted with a linear function to extract the gain of the pixel in units of LSB/mV. This is shown in Fig. 8(b) for an example pixel. A dedicated threshold scan around the noise floor is also executed. As one can see from the fit in Fig. 8(b), the test pulse voltage has an offset with respect to the baseline. The same effect is seen in other test pulse measurements and discussed in more detail in Sec. 4.1. Here, only the mean values of the gain are used to convert the noise measurements described in the following section into a voltage. Fig. 9 shows the offset and gain for all assemblies.

3.3. Noise Performance

To measure the noise, the threshold is scanned across the noise floor and the resulting distribution is fitted with a Gaussian. The mean of the Gaussian is defined as the baseline and the standard

[6] At even lower thresholds, a second s-curve can be seen. This is the result of the undershoot of the injected step voltage. Lowering the threshold even further, superimposes the injected pulses with the noise floor.

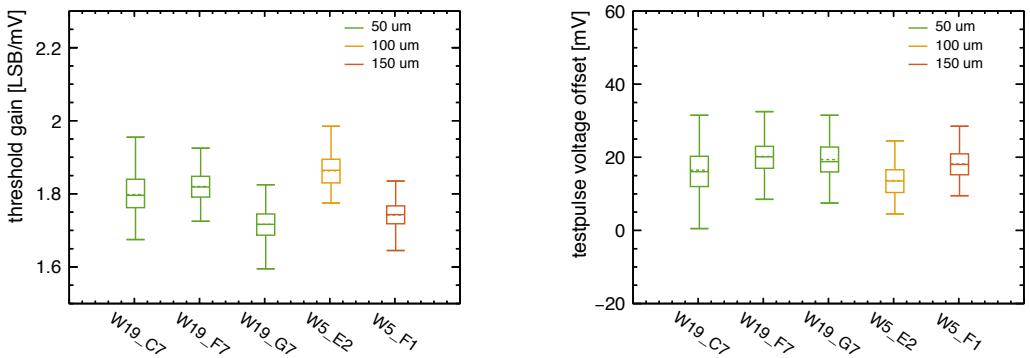

(a) (b)

Figure 9: Threshold gain (a) and offset (b) for all diagonal pixels as measured for the various assemblies. See Sec. 2.7 for the conventions used in this plot style.

deviation as the noise. Fig. 10 shows a map of the resulting values across the pixel matrix. While the baseline distribution appears random, the noise shows a clear pattern of 2x16 pixels which mirrors the digital building blocks of the ASIC, in which 4 super-pixels share common infrastructure.

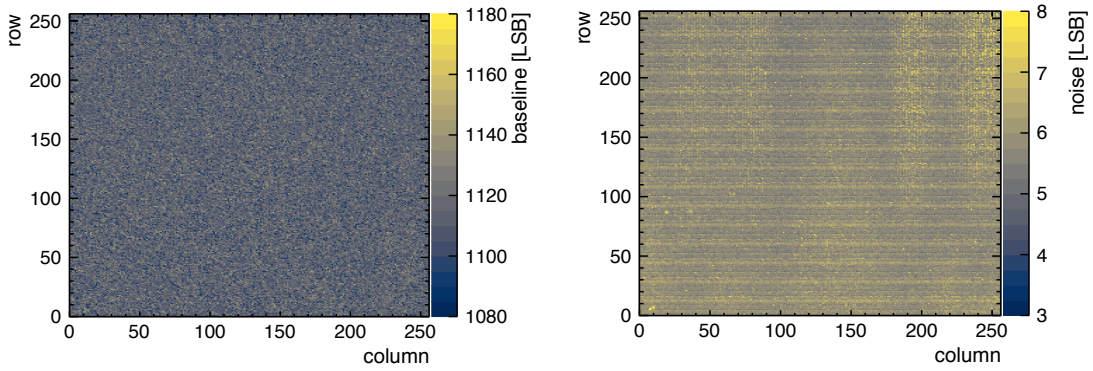

(a) (b)

Figure 10: Baseline (a) and noise distribution (b) after equalisation. Assembly shown is W5_E2.

Fig. 11 shows the noise for different ASICs before and after assembly with a sensor.[7] The values are given in units of electrons. The derivation of this conversion factor is described only later in Sec. 4 but is already used here for reasons of clarity. A small amount of additional noise is introduced by the assembly process but no correlation with the sensor capacitance or the leakage current could be found. The noise appears to be dominated by the intrinsic parameters of the ASIC. This is also supported by the fact that the noise is not affected significantly by a change in the operating temperature, measured on the ASIC, as is shown in Fig. 12(a). The noise is however affected by enabling the global Gray counter as can be seen in Fig. 12(b). This is relevant as the noise measurement is done in PC & iToT mode while normal data taking is

[7] Measurements before assembly are done at the wafer level with a dedicated probe-card.

done in ToT & ToA mode. The latter requires the Gray counter while the former does not and deactivates it by default, therefore reducing the noise. For this measurement the Gray counter was enabled manually.

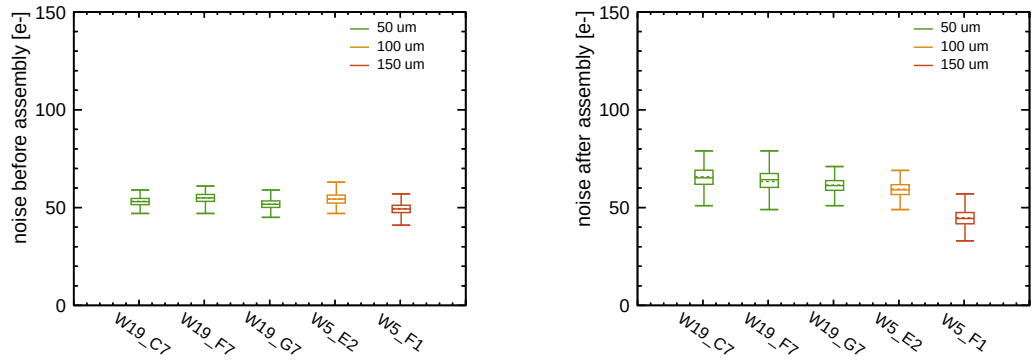

(a) (b)

Figure 11: Noise for all pixels of various ASICs before (a) and after (b) assembly. The noise is affected by the assembly process but not significantly by the sensor capacitance.

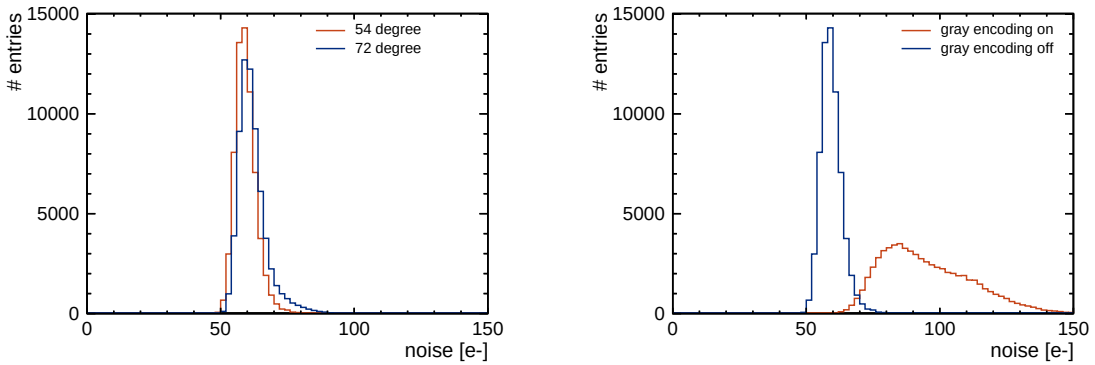

(a) (b)

Figure 12: Noise distribution of all pixels for different operating temperatures (a) and with and without activated Gray encoding (b). Assembly shown is W5_E2.

Based on the measurements described in this section, the nominal threshold values in Tab. 1 are chosen to be $6\,\sigma$ from the average baseline, where σ is the quadratic sum of the RMS of the distribution of all baselines for all pixels and the average noise without Gray counter of all pixels.

4. Calibration Procedure

4.1. Energy Calibration

The energy calibration of the assemblies is done in two steps. First, test pulse injection is used to finely sample the non-linear f_{tot} function and obtain a relative calibration from time-over-threshold to voltage. Then, an absolute calibration to energy is extracted via sources of known energy.

4.1.1. Time-Over-Treshold to Voltage Calibration

The calibration of f_{tot} is done via test pulse injection in ToT & ToA mode. Step voltages of various amplitudes are injected via the input capacitor. To avoid crosstalk, only 1 pixel in a 16 by 16 pixel sub-matrix is injected at the same time. Per step, 100 test pulses are injected while mean and standard deviation of the response are recorded as well as the number of detected pulses. Only sample points that detected all 100 pulses are selected for the fit. From that list, the point with the lowest amplitude is removed to limit noise effects. For the stability of the fitting process, it has proven useful to add a threshold estimation. Therefore, the midpoint between the last amplitude that recorded 0 and the first amplitude that recorded 100 pulses was added as threshold value with an uncertainty along the x-axis of the residuals to those two points. The result is fitted with Eq. 2. An exemplary fit can be seen in Fig. 13.

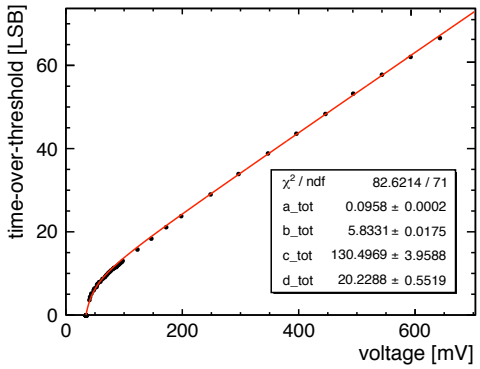

Figure 13: Single pixel example fit of the time-over-threshold response measured with test pulses. From assembly W19_C7.

Later, the inverse function of Eq. 2,

$$f_{tot}^{-1}(x) = \frac{a_{tot}t_{tot} + x - b_{tot} + \sqrt{(b_{tot} + a_{tot}t_{tot} - x)^2 + 4a_{tot}c_{tot}}}{2a_{tot}}, \tag{4}$$

is used to convert ToT values to voltage. The extracted parameters of the ToT response for all assemblies are shown in Fig. 14. From Fig. 14(a) one can see that the spread of the ToT gain is systematically smaller for the three assemblies from wafer 19 than for the other assemblies from wafer 5. This is more prominent if one looks at the variation of this value across the matrix as shown in Fig. 15 for 2 examples. While the ASICs from wafer 5 show larger scale structures across the matrix, the ASICs from wafer 19 appear to show only random variations. This is due to a change in the power distribution of the discharge current that was implemented from wafer 13 onwards.

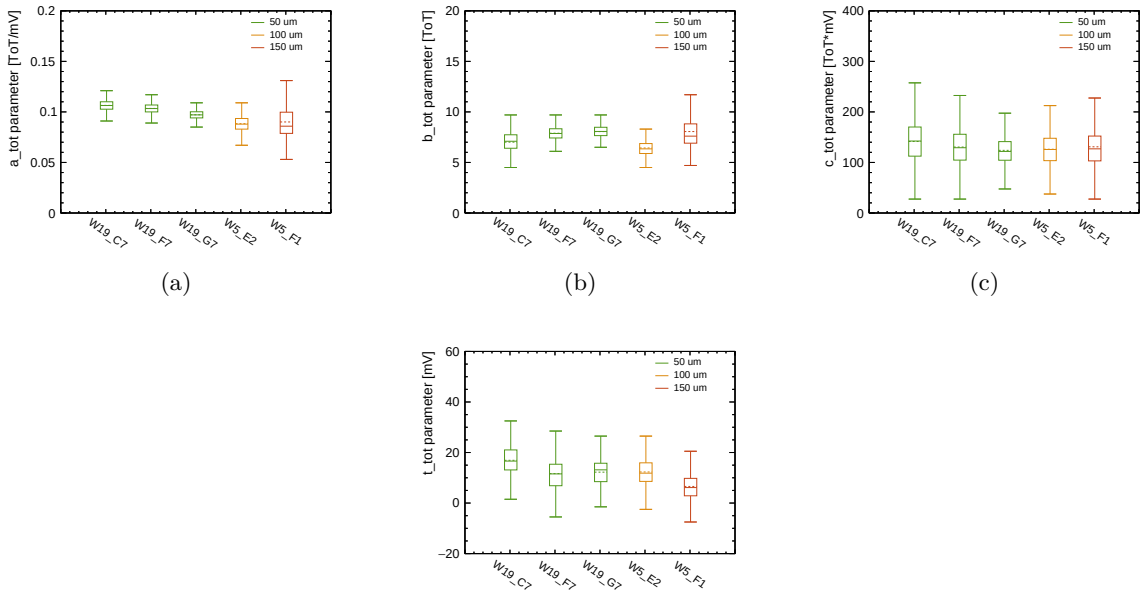

(a) (b) (c)

(d)

Figure 14: ToT calibration parameters for 5 different assemblies.

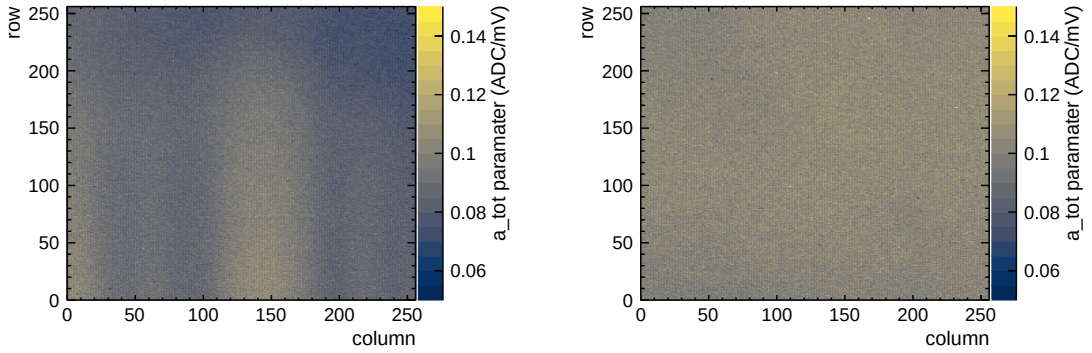

(a) W5_E2 (b) W19_C7

Figure 15: The gain in units of ADC per mV for an ASIC from wafer 5 (a) and from wafer 19 (b).

4.1.2. Voltage to Energy Calibration

For the absolute energy calibration, fluorescent x-rays from an electron tube are used with the setup described in Sec. 2.5. The x-rays enter from the sensor backside. The target materials used and their relevant energy lines are listed in Tab. 2. The values are averaged Kα lines, weighted by their intensity according to [8]. To limit the effect of sub-threshold energy depositions, only single pixel clusters are considered. All assemblies are calibrated by Fe and In targets. Other targets are used for verification only. Per pixel and target, 500 events are required for a per-pixel calibration. Pixels with fewer events are assigned a global average value.

The peaks of the known energy lines are then used to obtain an absolute energy calibration.

Table 2: List of x-ray targets and their corresponding energy used for this study. Energies are weighted with intensities according to [8].

Target Element [-]	Kα Energy [keV]	Attenuation Length (Si,300K) [mm]
Fe	6.40	0.034
Cu	8.04	0.066
Pb	10.55 (Lα)	0.14
Zr	15.77	0.43
In	24.14	1.40

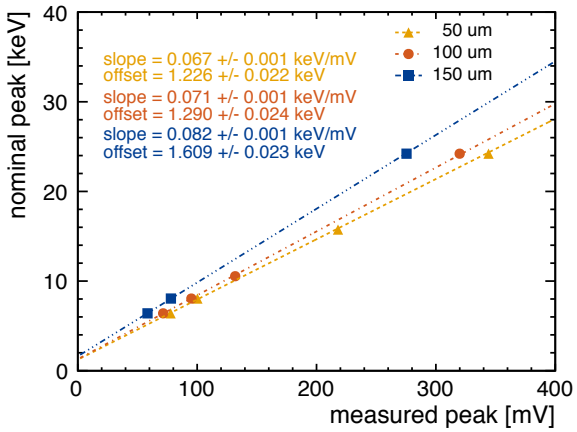

Figure 16: Nominal peak position in energy vs. measured peak position in voltage. The three assemblies show a different slope and an offset different from 0.

This procedure is shown in Fig. 16 for the global spectra. One would assume a direct proportionality that is determined by the test pulse input capacitor. The observed behaviour is indeed linear but shows an offset. The same behaviour is also observed in the threshold gain calibration with test pulses described Sec. 3.2. From this observation follows, that two parameters are necessary for a full absolute calibration.

$$f_{\text{volt}}(x) = a_{\text{volt}}x + b_{\text{volt}} \tag{5}$$

The extracted parameters for all assemblies are shown in Fig. 17. The charge scale is obtained by dividing the energy by 3.65 eV [9], the average energy needed to create one free charge carrier pair in silicon.

The a_{volt} parameter corresponds to a capacitance in units of [e-/mV] which in turn corresponds to [0.16 fF]. This value should be equal to the value of the capacitance used for the test pulse injection. The design value of 3 fF or 18.75 e-/mV is in good agreement with the values measured for the 50 µm sensor but is about 20% smaller than the values measured for the 150 µm sensor. Whether this discrepance results from an underestimation of the x-ray energy scale due to sub-threshold charge sharing or is of different origin will require future studies. The b_{volt} parameter corresponds to an offset in [e-]. When interpreting the absolute value of these two

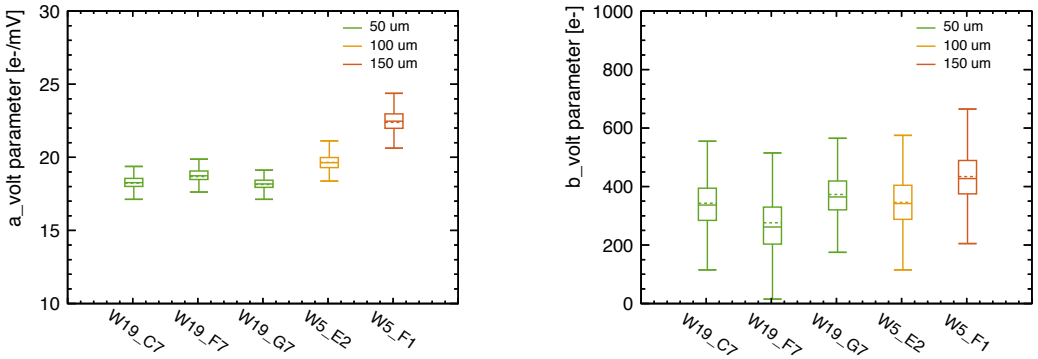

(a) (b)

Figure 17: Voltage calibration parameters for all pixels and 5 different assemblies.

parameters, one should keep in mind that the voltage is measured at the periphery of the ASIC and not at the pixel itself. Possible losses due to e.g. the signal routing or cross talk are not identifiable. Therefore, the voltage scale should only be seen as an intermediate step towards the final calibration scale which is in [e-] and measured with x-ray sources of known energy.

4.1.3. Verification of the Energy Calibration

With a full absolute calibration pixel-by-pixel, the global energy response is analysed again. The result is shown in Fig. 18. All peaks are now located at the expected position. It should be pointed out that the Fe and In peaks are used for the calibration while the Cu, Pb and Zr measurements are independent and only used for verification purposes.

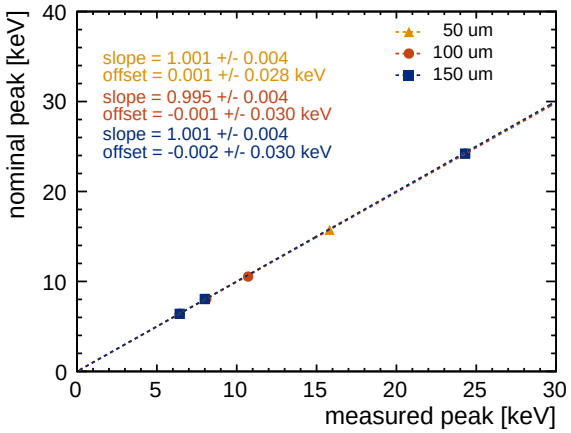

Figure 18: Nominal peak energy vs. measured peak position in energy. Fe and In points are used for calibration, while the Cu, Pb and Zr points are added for verification purposes.

Table 3: Average values for effective threshold and noise parameters for all assemblies.

Chip ID [-]	Threshold RMS [e-]	Avg. Noise Gray Code Off [e-]	Avg. Noise Gray Code On [e-]	Eff. Threshold [e-]
W19_C7	89	66	90	924
W19_F7	72	64	89	815
W19_G7	82	64	91	849
W5_E2	76	61	96	895
W5_F1	79	57	86	913

4.1.4. Effective Threshold and Noise

From the test pulse calibration one can also extract the effective threshold by fitting a CDF to the region in which the number of detected test pulses goes from 0 to 100, similarly as it is done in Sec. 3.2 for the threshold gain calibration. The result can be seen in Fig. 19(a). The average value across all assemblies is around 880 electrons.

The effective noise with activated Gray encoding per assembly is shown in Fig. 19(b) in units of [e-]. The average value is around 90 electrons. The average noise and threshold values for all assemblies can be found in Tab. 3.

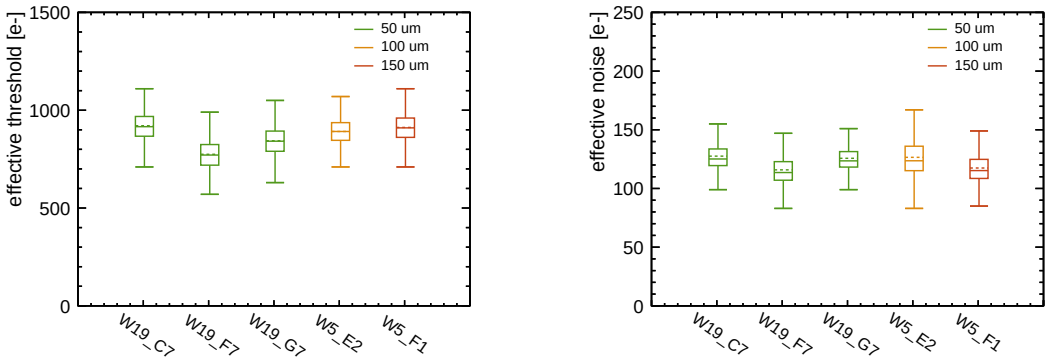

(a) (b)

Figure 19: Effective threshold and noise values for all pixels and 5 different assemblies.

4.2. Time Calibration

Similar to the energy calibration, the time calibration is done in two steps by a combination of test pulses for the non-linear timewalk and beam data to calibrate the delay.

4.2.1. Timewalk Calibration

The calibration of f_{toa} is done by first injecting a test pulse directly into the digital frontend that is not affected by timewalk and after a fixed delay a second, analog test pulse of varying

amplitude. The ToA values of both pulses are recorded and the time difference is calculated. A shift of the 640 MHz clock of one cycle per double column has to be taken into account. This procedure is repeated 100 times for various amplitudes for the second pulse and the dependence of time difference on the injected amplitude is recorded. The injection scheme is identical to the ToT calibration. The resulting curve is then fitted with Eq. 1. An exemplary data curve and fit can be seen in Fig. 20.

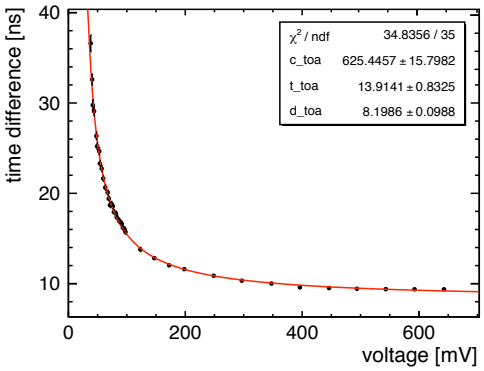

Figure 20: Example fit of the timewalk measured with test pulses for a single pixel. From assembly W19_C7.

The extracted parameters of the timewalk response for all assemblies are shown in Fig. 21. The ranges of the parameters have not been restricted and therefore also negative values for t_{toa} are possible. It should be noted that it is also possible to do the calibration directly with ToT data, in case the energy calibration is not required.

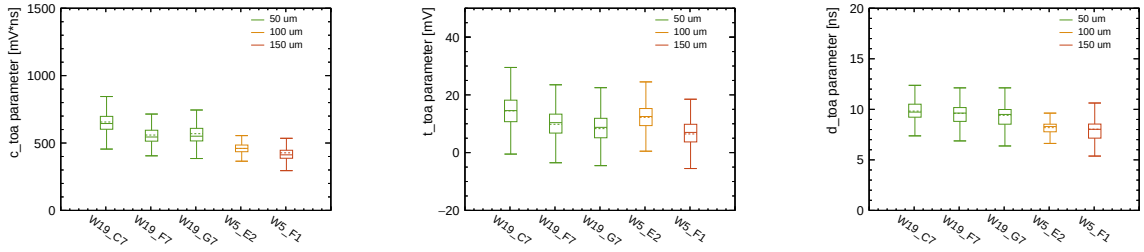

(a) (b) (c)

Figure 21: ToA calibration parameters for all pixels and 5 different assemblies.

4.2.2. Delay Calibration

The timewalk calibration also includes a delay with the d_{toa} parameter. However, as the test pulse injection uses the same clock as the ToA, any variation in the clock distribution between pixels can not be detected this way. To calibrate these offsets in time, beam tests have been conducted in the setup described in Sec. 2.6.

Fig. 22(a) shows the mean time difference between scintillator and DUT across the pixel matrix. These values are used to obtain a pixel by pixel offset calibration. Qualitatively,

structures with a period of 16 double columns can be observed and a tendency of later timestamps from higher row numbers. The latter is expected as the clock propagation along one column is expected to take about 1.5 ns between the top and the bottom row. This number is roughly observed. Fig. 22(b) shows the RMS for the same distributions. Here, larger values every 16 rows can be correlated to larger noise values that were also observed for these rows.

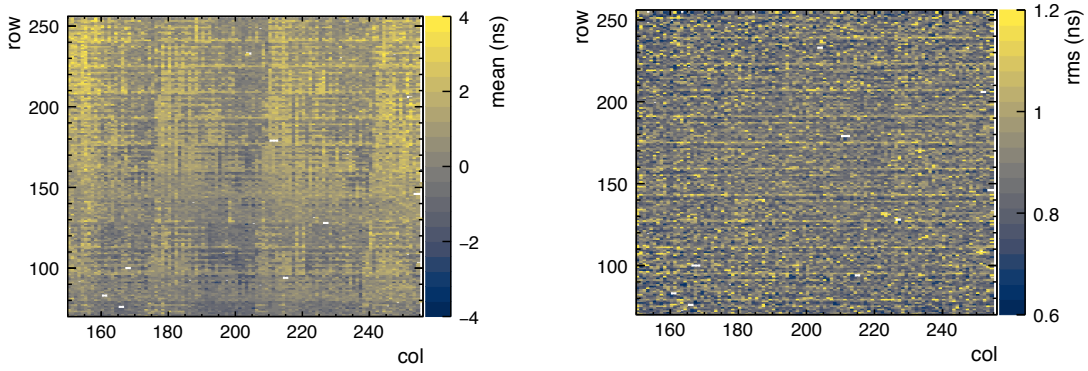

(a) (b)

Figure 22: Mean and RMS of the time difference between DUT and scintillator across the pixel matrix.

5. Impact of the Calibration

5.1. Uniformity of Responses

Fig. 23 shows the most probable value of the Zr Kα line, located about midway between the two calibration points, for the absolute calibration and with relative calibration only. The uniformity is much improved when using the absolute calibration and the 16 x 2 pattern has disappeared. Across the matrix, the relative dispersion is reduced from 6.6% to 5.3%. Only pixels with more than 100 events within the region of interest are considered.

5.2. Impact on Energy Measurements

As an example, a global Fe spectrum in time-over-threshold, voltage and energy is shown in Fig. 24. The time-over-threshold spectrum is non-linear and the pixel response is not yet equalised. No fit to the peak is attempted. Converting the spectrum to a voltage, linearises the x scale and results in a Gaussian peak. The absolute calibration improves the resolution and results in a more distinct threshold. This becomes more evident when looking at Fig. 25 which shows the resolution as function of x-ray energy. For all energies, the resolution is improved. At the 6.40 keV Fe line, the resolution is 9.3 %.

5.3. Impact on Time Measurements

For thin silicon sensors, the effect of timewalk is significantly increased due to the small energy deposition of minimum ionising particles.

This can be understood from Fig. 26(a) which shows the mean and RMS of the measured timewalk averaged over all pixels. While the mean timewalk can be corrected with the proced-

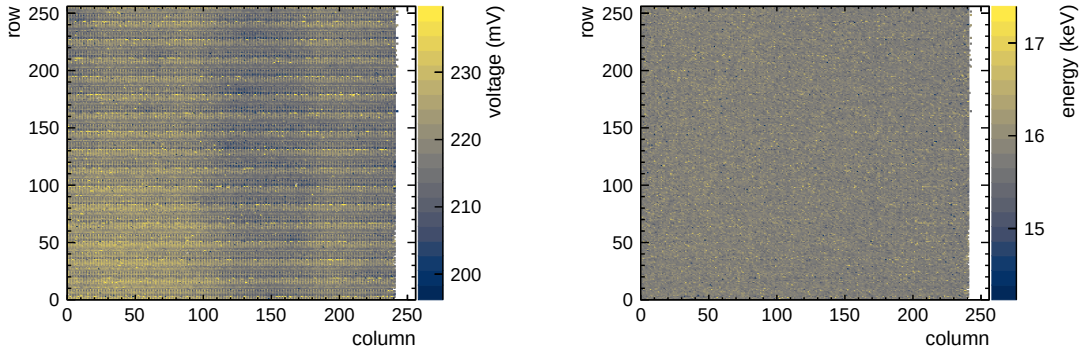

(a) (b)

Figure 23: Most probable value of the Zr Kα line before (a) and after (b) the absolute calibration. Assembly shown is W19_C7.

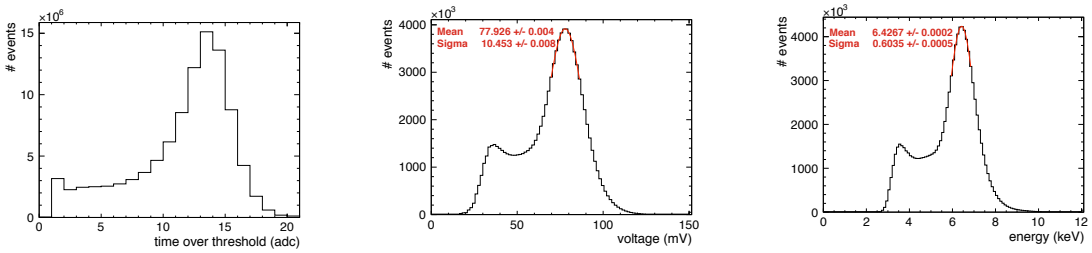

(a) (b) (c)

Figure 24: Recorded fluorescence spectrum of Fe with events from all individual pixels. The ToT spectrum (a) is non-linear, no peak fit is attempted. Calibration to voltage (b) and energy (c) corrects for the non-linearities and improves the resolution by equalising the response across the matrix. Shown assembly is W19_C7.

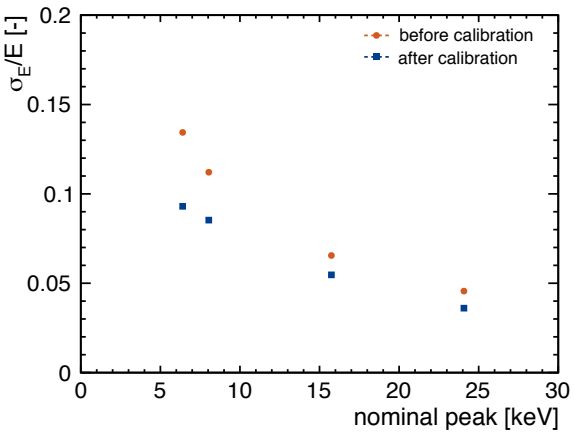

Figure 25: Energy resolution before and after absolute calibration for various x-ray energies. Shown assembly is W19_C7.

ure layed out in Sec. 4.2, the RMS of the timewalk is an irreducible contribution to the time resolution. It decreases with increasing pulse height reaching a constant of about 420 ps. It should be pointed out that this is not the limit due to bin size of the fast ToA clock running at 640 MHz. The test pulses injection is not randomised and occurs always at the same clock phase. Rather, this is the jitter of the discriminator and the amplifier due to noise and rise time. This value is in agreement with simulations of the ASIC design. Also, the clock binning of b = 1.56 ns is expected to contribute a constant term of $\frac{b}{\sqrt{12}}$. The contributions from jitter and finite clock binning as well as the contribution of both added in quadrature are shown in Fig. 26(b) with a constant term of about 620 ps. Theoretically, this is the expected contribution of the electronics on the time resolution. It should be kept in mind however that possible clock non-uniformities, especially with the 640 MHz clock, can degrade this resolution.

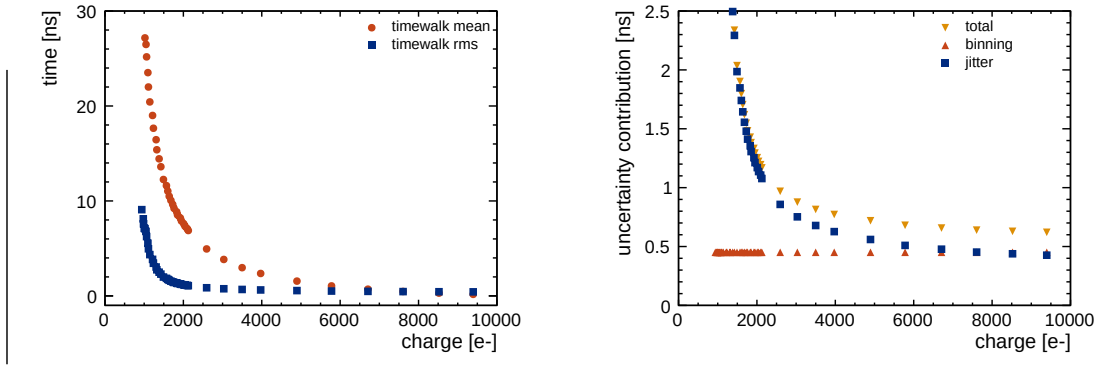

(a) (b)

Figure 26: Mean and RMS of the measured time delay per pixel from 100 injected test pulses per amplitude (a). While the mean timewalk can be corrected, the RMS of the timewalk due to noise is irreducible and contributes to the final time resolution. (b) shows the expected contributions from jitter and binning of the fast ToA clock.

The total time resolution including sensor contributions is measured in particle beams with the setup described in Sec. 2.6. From the three obtained timestamps of track, DUT and scintillator, three time differences and consequently uncertainties of these can be obtained. Assuming they are not correlated, these three equations with three variables can be solved uniquely and the resolution of the scintillator can be extracted from the measured histograms of the time differences.

$$\sigma_{t_{ref}} = \sqrt{-\frac{1}{2}(\sigma^2_{t_{track}-t_{dut}} - \sigma^2_{t_{dut}-t_{ref}} - \sigma^2_{t_{ref}-t_{track}})} \tag{6}$$

Indeed, the three time differences in Eq. 6 are not completely independent because they all run on the same clock supplied by the TLU. However, due to the much finer binning of the TDC that measures the scintillator as well as the combination of multiple timestamps, each with a delay from time-of-flight as well as the latency, the correlation is assumed to be negligible. Eq. 6 is used independently for all analysed runs and the average extracted resolution of the scintillator is

$$\sigma_{\text{ref}} = 0.30 \pm 0.04 \text{ ns}$$

In a similar way, the track time resolution, without any applied calibration, of the 6 telescope planes can be extracted as

$$\sigma_{\text{track}} = 1.11 \pm 0.03 \text{ ns}$$

The DUT resolution is defined as the RMS of the residual distribution between scintillator timestamp and DUT with the scintillator resolution subtracted in quadrature.

$$\sigma_{\text{dut}} = \sqrt{\text{RMS}^2_{t_{ref}-t_{dut}} - \sigma^2_{\text{ref}}} \tag{7}$$

The uncertainty on the RMS is estimated as 0.03 ns from three different 50 µm assemblies measured at 15 V. The propagated uncertainty on the time resolution σ_{dut} is 0.04 ns.

Fig. 27 shows the time resolution obtained in beam tests with 120 GeV pions for 3 different assemblies. A significant improvement in the resolution can be seen due to the timewalk correction for the 50 µm sensor. The improvement is then reduced when moving to thicker sensors due to the larger energy deposits. After timewalk correction, all sensors yield approximately the same resolution at their nominal operating voltage.

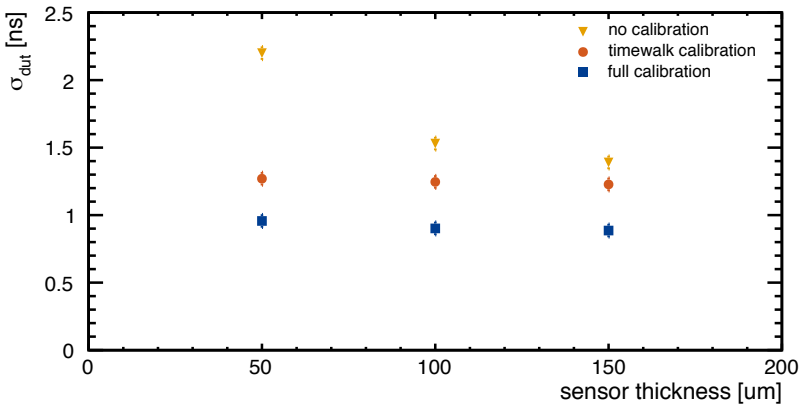

Figure 27: Time resolution with and without corrections for different sensor thicknesses measured in beams with 120 GeV pions. The reference timestamp is taken with an organic scintillating read out by a PMT. Its resolution of 0.3 ns is deconvoluted.

Fig. 28 shows the extracted time difference as function of the signal amplitude before and after the calibration procedure described in Sec. 4.2. Except for the very smallest amplitudes, no timewalk is visible anymore.

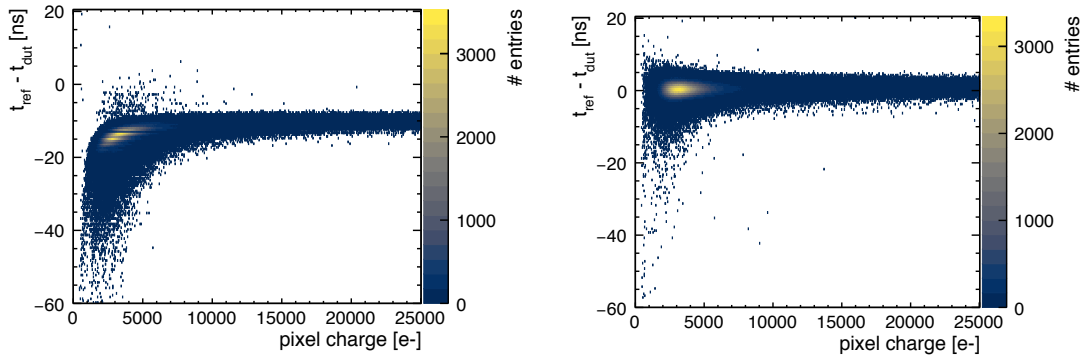

(a) (b)

Figure 28: Timewalk before (a) and after (b) applied corrections for a 50 µm thick sensor.

The electric field has a strong influence on the time resolution as well. Fig. 29 shows the obtained time resolution for different bias voltages for the 50 µm and 150 µm sensor which deplete at around 10 V and 25 V respectively. The resolution however is improving beyond that point due to stronger electric field at higher bias voltages. This is due to an increase in the drift velocity that in turn results in a faster signal creation on the CSA input. A slightly better resolution can be observed for the 150 µm sensor at the highest bias. Due to the larger average charge deposition, this is in good agreement with the expectations from Fig. 26(b). The best value for the time resolution reached in this study is

$$0.72 \pm 0.04 \text{ ns}$$

Fig. 30 shows the histograms for the highest bias voltages of the two thicknesses at the various calibration stages.

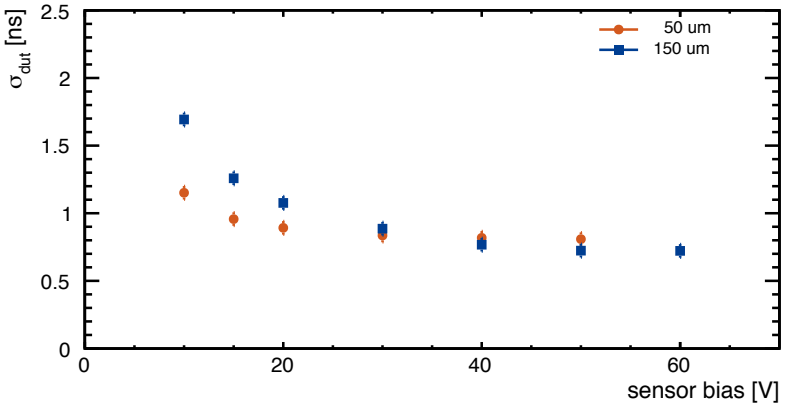

Figure 29: Time resolution at different bias voltage. An improvement beyond full depletion can be seen due to stronger electric fields.

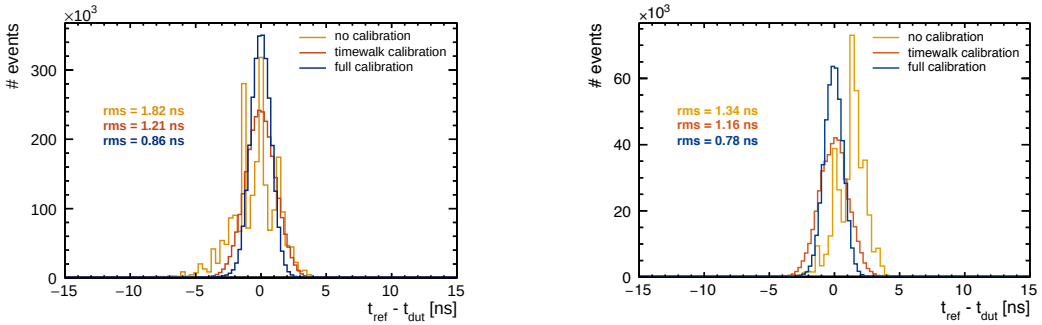

(a) (b)

Figure 30: Example histograms for (a) 50 µm at 50 V and (b) 150 µm at 60 V for different calibration stages. From the RMS values, 0.3 ns are deconvoluted to obtain the time resolution.

6. Summary and Conclusions

In this work, a time efficient method for pixel-by-pixel calibration of the Timepix3 ASIC has been presented. Five assemblies of Timepix3 ASICs bumb-bonded to thin silicon pixel sensors of thicknesses between 50 and 150 µm were calibrated and measured. Results on threshold equalisation, gain dispersion and noise are shown. After calibration, the energy resolution at 6.40 keV is 9.3 %. For 120 GeV pions, time resolutions down to 0.72 ns are achieved.

Acknowledgements

The authors thank Fernando Duarte Ramos (CERN) for his support with the mechanical integration of the tested devices in the telescope system. The help from the staff operating the CERN SPS and the North Area test facilities is gratefully acknowledged. This project has received funding from the European Union's Horizon 2020 Research and Innovation programme under Grant Agreement no. 654168 and from the Austrian Doctoral Student Programme at CERN.

References

[1] T. Poikela et al., *Timepix3: a 65K channel hybrid pixel readout chip with simultaneous ToA/ToT and sparse readout*, Journal of Instrumentation **9** (2014) C05013, DOI: 10.1088/1748-0221/9/05/C05013.

[2] F. Krummenacher, *Pixel detectors with local intelligence: an IC designer point of view*, Nuclear Instruments and Methods in Physics Research Section A: Accelerators, Spectrometers, Detectors and Associated Equipment **305** (1991) 527, ISSN: 0168-9002, DOI: 10.1016/0168-9002(91)90152-G.

[3] M. D. Gaspari et al., *Design of the analog front-end for the Timepix3 and Smallpix hybrid pixel detectors in 130 nm CMOS technology*, Journal of Instrumentation **9** (2014) C01037, DOI: 10.1088/1748-0221/9/01/C01037.

[4] J. Visser et al., *SPIDR: a read-out system for Medipix3 and Timepix3*, Journal of Instrumentation **10** (2015) C12028, DOI: 10.1088/1748-0221/10/12/C12028.

[5] N. A. Tehrani, *Test-beam measurements and simulation studies of thin pixel sensors for the CLIC vertex detector*, PhD thesis, ETH Zürich, 2017, DOI: 10.3929/ethz-b-000164813.

[6] *Corryvreckan*, URL: https://gitlab.cern.ch/corryvreckan.

[7] *Wikipedia*, last accessed 21.03.2018, URL: https://en.wikipedia.org/wiki/Box_plot.

[8] *Lawrence Berkeley National Laboratory: The X-Ray data booklet*, last accessed 21.03.2018, URL: https://xdb.lbl.gov.

[9] G. Fraser et al., *The X-ray energy response of silicon Part A. Theory*, Nuclear Instruments and Methods in Physics Research Section A: Accelerators, Spectrometers, Detectors and Associated Equipment **350** (1994) 368, ISSN: 0168-9002, DOI: 10.1016/0168-9002(94)91185-1.

Appendices

A. Derivation of Timewalk and Time-over-Threshold Response Function

Consider an event with amplitude x occurring at time t_0. The time t_0' when the amplitude crosses a constant threshold value x_{thr} is recorded. Due to the finite and constant rise time t_{rise} of the system, this timestamp is shifted in time by an amount that depends on the signal amplitude

$$t_0' = t_0 + \Delta t$$

This is sketched in fig. 31.

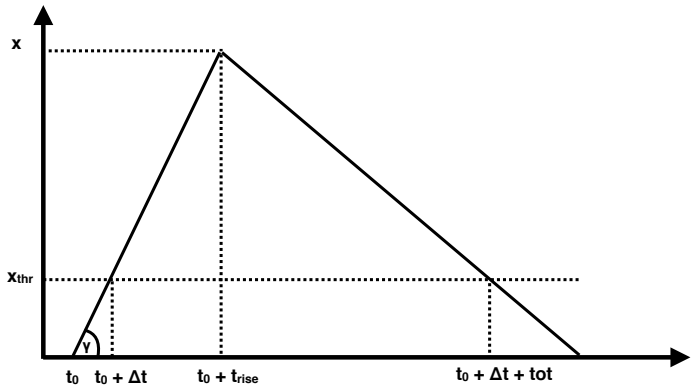

Figure 31: Sketch of the timewalk and time over threshold principle.

Assuming a linear rise and fall, the following relations holds.

$$\tan\gamma = \frac{x_{\text{thr}}}{\Delta t} = \frac{x}{t_{\text{rise}}}$$

Both x_{thr} and t_{rise} are system constants. With the possibility of a constant delay and a shifted amplitude scale x', the time shift can then be expressed as

$$\Delta t = \frac{c_0}{x' - c_1} + c_2 \tag{8}$$

The time-over-threshold before the peaking time is then $t_{\text{rise}} - \Delta t$. Assuming also a constant discharge rate, the time to discharge the capacitor is linear and total time over threshold

$$\text{tot} = \frac{c_0}{x' - c_1} + c_3 x' + c_4 \tag{9}$$

In reality, the signal shape is not a perfect triangle. The rising edge is not fully linear and the discharge already starts as soon as there is a potential difference across the CSA. However, for Timepix3 the rise time of 25 ns is much faster than the discharge and the functions derived here fit quite well.